Quantifying Development: Using T_2 Relaxation to Investigate Myelination of the Corpus Callosum in Preadolescents

by

Kirstie Jane Whitaker

A thesis submitted in partial fulfillment of the requirements for the degree of

Master of Science

in

The Faculty of Graduate Studies

(Physics)

The University of British Columbia

(Vancouver)

September 2010

Abstract

This thesis describes a novel voxel-based analysis of the transverse (T_2) relaxation decay curve to quantify myelin water fraction (MWF). Multi-echo T_2 relaxation decay data was acquired for 5 preadolescent males (age range 9 – 12 years). A novel signal to noise filter appropriate for multi-exponential T_2 analysis was then applied to remove voxels which did not accurately fit the modelled curve. The remaining voxels were designated "highly myelinated" if their MWF was greater than a certain critical value. A range of signal to noise filter cut-off values and highly myelinated critical values were investigated. This thesis demonstrates, for the first time, a very strong and significant correlation ($r = 0.990$, $p = 0.001$) between verbal intelligence quotient scores on the Wechsler Intelligence Scale for Children – Revised and myelination in the corpus callosum of developing children. This relationship is supported by a growing number of studies showing a correlation between white matter development and cognitive ability. In addition, due to the restricted age range of our subjects, this work is able to show the individual variations in myelin maturation rates.

Table of Contents

List of Figures

Acknowledgments

Thanks must go, first and foremost, to my supervisors, Dr Alex Mackay and Dr Campbell Clark. Both taught me more than I could have predicted and have irrevocably shaped my future for the better. Their influence only becomes stronger with time. They supported me through an academic adolescence, where I didn't know what I wanted to do, or, if something did occur to me, how to do it. And more often than not I solved this with a ski trip or ten. The completion of this thesis marks a transition in my career, and I hope that my future work will do them proud.

The person who has really made this study happen is Shannon Kolind. She taught me everything I needed to know in the field of MRI data analysis; from how to open matlab to writing the code for these analyses, and everything in between. Her contribution in writing up this work for publication was invaluable, and her collection of rubber duckies will always make me smile.

The data for this work was actually collected, before my time, by Craig Jones and Heike Dumke, and I thank them for their hard work. Of course there would be no thesis without the subjects, children I never met but whose brains I stared at for months on end, and I'm grateful for their participation in a loud and often scary brain scan.

Finally, there are those outside the lab: my money, my family and my friends. I was funded at UBC by a Commonwealth Scholarship, and I owe my wonderful three years in Canada to their generosity. Of course, I can never adequately express how well my family and friends looked after me. They welcomed me to a new country, joined me on adventures to mountains and seashores, lifted me up and supported me through all the tough times. Those vanilla lattes and long distance phone calls did more to raise my spirits than you can possibly know.

Thank you.

1 Introduction, Background and Motivation

One of the primary goals of the neurosciences is to understand the biological underpinnings of human cognitive and emotional development. Following Sherrington's lead, the proposed models from the last century of work have primarily concentrated on the synapse. Although neuronal development and communication is clearly a necessary function for models of human development, work in the past decade has demonstrated that it is insufficient to fully explain the phenomena.

This belief arises from the recognition that models of neuronal firing cannot fully explain the dramatic and sequential acquisition of abilities that characterise normal human development during the first two decades of life. At birth, when the neonate is essentially defenceless and completely dependent on others for succour, the majority of neuronal proliferation, migration and specialisation are complete. Subsequently, more complex behaviours develop in a sequential manner. The maturation rates within this pattern of development vary across individuals, while the pattern itself remains consistent within the species.

From a logical point of view, a suggested biological mechanism to complement the neuronal model for explaining mental functions and development should fulfil the following criteria:

1. Provide a rationale for its impact on cell firing
2. Exhibit measurable changes in regions of the brain associated with specific abilities

3. These changes should be temporally consistent with the acquisition of specific abilities
4. The rates of change should vary across individuals and hence reflect the variation in behavioural observed across people of the same age.

Myelination of neuronal axons has been suggested by many as a mechanism that meets the above criteria. This chapter outlines the structure and function of myelin, how myelin can be imaged using magnetic resonance (MR) techniques and the current base of knowledge regarding its development. With this information in mind, the criteria above are revisited at the end of this chapter and specific hypotheses for this study are described.

1.1.1 Myelin: Structure and Function

Myelin is found in both the central and peripheral nervous systems of vertebrates. It is a lipid-protein lamellar membranous structure which surrounds neuronal axons. In the central nervous system (CNS) it is responsible for white matter's characteristic colour and makes up approximately 50% of its mass. Grey matter does contain myelin but in much lower quantities.

Figure 1-1 illustrates a myelinated axon. The myelin bilayer comprises approximately 80% lipid and 20% protein and approximately 40% (by weight) of the space between the bilayers is water. The myelin of the CNS is produced by oligodendrocytes and the bilayers illustrated are made up of oligodendrocyte cell membranes.

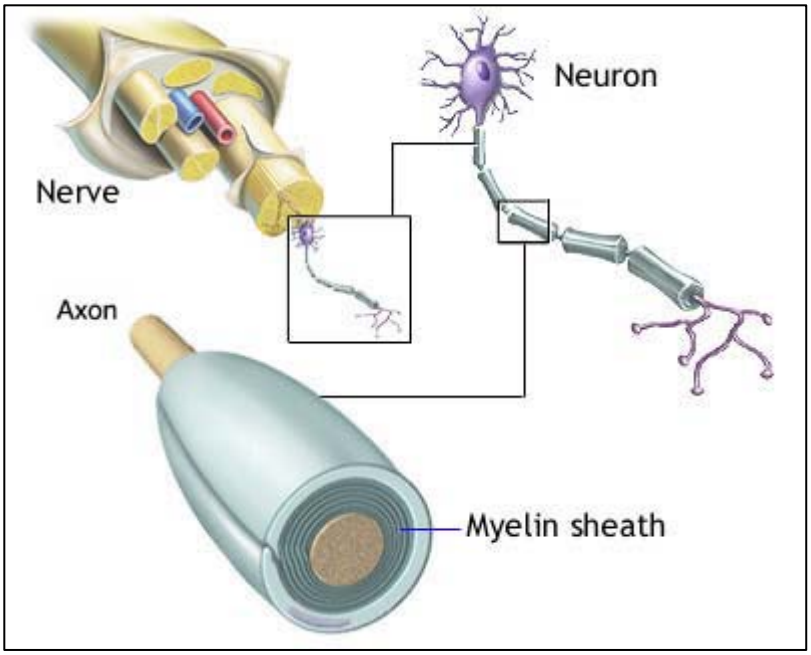

Figure 1-1 Conceptual illustration of myelin and nerve structure [1].

Unmyelinated axons transmit action potentials using continuous conduction mediated by sodium channels arranged along the length of the axon, while myelinated axons transmit these electrical messages by saltatory conduction. Saltatory conduction is characterised by the depolarisation of a whole section between two successive nodes of Ranvier, which mark a gap in the myelin sheath and the location of the voltage-gated sodium channels. Since the areas wrapped in the myelin sheath are electrically insulated the action potential jumps from one node of Ranvier to the next and thus allows much faster conduction. This increased transmission speed of signals is necessary for complex functions, such as those associated with motor, sensory and behavioural processes.

Recent developments in molecular and systems neuroscience have illustrated the critical role which white matter plays in physiological mechanisms of brain maturation and neural

signalling [2-6]. Therefore we can be confident that techniques which allow more precise and accurate imaging of myelinated fibres will allow a better investigation and understanding of the white matter of the CNS.

1.1.2 Myelin Imaging

Five techniques are currently utilised to image myelin. Currently it is not possible, at a clinically relevant level, to image the non-aqueous proteins and lipids which make up myelin not only due to the very fast signal decay time but also the difficulty (in fact, near impossibility) in distinguishing specific myelin molecules from the other non aqueous tissue surrounding them.

Therefore, to investigate myelin in vivo, an indirect measure of myelin is provided though the imaging of the water in the CNS. Four methods are summarised in this section and the investigation of myelin using T_2 relaxation, the technique used to image myelin in this thesis, is described in detail.

1.1.3 Quantitative T_2 Relaxation

As described in detail in the following chapter (section 2.5) T_2 relaxation can be analysed to consider the relative number of protons in any number of water environments. In fact, data from normal CNS tissue resolves remarkably consistent T_2 distributions which illustrate three peaks representing three water environments. An example is shown in figure 1-2.

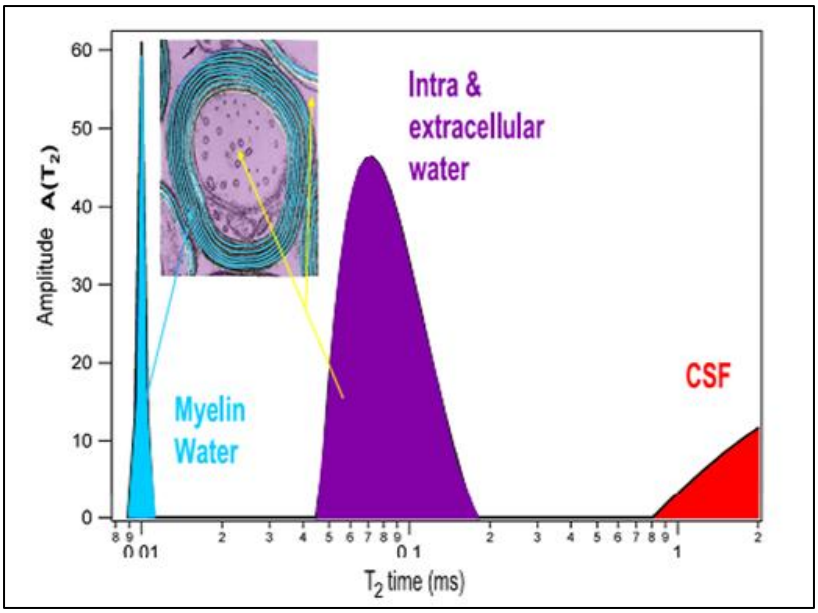

Figure 1-2: Typical T_2 distribution of central nervous system tissue. The three water environments with distinct spin-spin relaxation times are illustrated representing myelin water, intra and extra cellular water and cerebrospinal fluid. Inset is an electron micrograph of a myelinated axon in cross section. (Figure reproduced courtesy of Cornelia Laule.)

The three peaks illustrated in figure 1-2 have been assigned to cerebrospinal fluid CSF, intra and extra cellular water, and water trapped between the myelin bilayers or "myelin water" [7, 8]. The myelin water is the most constrained and therefore has the shortest T_2 time, while the CSF represents the least inhibited environment and therefore demonstrates a T_2 time close to that of free water.

Histopathological work which correlates the relative amount of myelin water (myelin water fraction, or MWF) to tissue stained for phospholipid components of myelin has supported the hypothesis that T_2 relaxation can provide an indirect but reliably quantitative measure of myelin in CNS white matter [9-14]. MR studies have detected the short T_2 component in myelinated trigeminal and optic nerves of the garfish, but not in the

same species' unmyelinated olfactory nerve [15], lending credence to the specificity of the short T_2 component to myelin.

One drawbacks of the T_2 relaxation technique is the very high signal to noise ratio required to accurately compute the T_2 distribution. Another is the 30 minutes of scan time required to amass the data from just one slice. However, although this thesis does not consider new approaches to data acquisition, work by Oh [16] and [17][17][17]Mädler and Kolind [18] is drastically reducing the acquisition time required to produce three dimensional images using this technique.

1.1.4 Alternative Techniques for the Magnetic Resonance Imaging of Myelin

Conventional Magnetic Resonance Imaging

T_1 and T_2 weighted imaging has been used in studies of myelin development in neonates and very young children. This technique, which highlights areas with long relaxation times (either longitudinal or transverse depending on the pulse sequence utilised) as hyperintense, is solely qualitative. While decreases in T_1 and T_2 times of the developing brain have been significantly correlated with decreases in water content [19], which may represent an increase in myelin, the assumption that myelination is the only process changing in the CNS at this time is naïve and is not considered a viable assessment of myelin content in children over 1 year of age.

MR Spectroscopy

MR Spectroscopy (MRS) can be used to illustrate the concentration of certain lipids and provides indirect information about myelin concentration [20]. Myelin development has been imaged using proton MRS [21, 22]. Unfortunately the low signal to noise ratio of MRS renders it insufficiently sensitive to normal myelin development in older children and adolescents. However, this technique is quickly advancing and may prove to become important in future research.

Diffusion Tensor Imaging

Diffusion Tensor Imaging (DTI) is an MRI technique which enables the measurement of the restricted diffusion of water in tissue. This is achieved by applying gradients in at least 6 directions and analysing the tensor which describes the three dimensional shape of the diffusion for each voxel. The mean diffusivity, <D>, and the fractional anisotropy (FA) can be calculated, along with the axial and radial eigenvalues ($\lambda_{//}$ and $\lambda_{\perp}$ respectively) of the tensor. These measures can be used to track white matter tracts in the brain (tractography) and has been shown to be a quantitative measure of myelin in animal models [23, 24].

This method is the most utilised to image myelin development and the vast body of literature which investigates myelin development in children and young adults uses DTI (see section 1.3). We should not find it difficult to believe that the insulation of an axon which myelin provides will affect the anisotropy of water diffusion; however, it is well know that myelin is not necessary for this anisotropy to occur. Work by Beaulieu *et al* [25] has shown that changes in DTI measures with age can be attributed to increases in fibre

diameter, greater cohesiveness and compactness of the fibre tracts, reduced extra-axonal spaces and a reduction in brain water, along with changes in myelin density. This work is supported by Schmithorst *et al* [26] and Suzuki *et al* [19]. It is, therefore, more appropriate to utilise DTI in the investigation of changes in myelination, rather than an absolute measure since it is not possible to resolve single axons in human CNS tissue at a clinical level and fibre tract orientation within the imaging voxel strongly affects the tensor.

Magnetisation Transfer

Magnetisation transfer imaging looks at the exchange of magnetisation between water and non-aqueous tissue [27]. A magnetisation transfer ratio (MTR) is usually calculated although other tissue parameters can be obtained, such as the fraction of protons on non aqueous tissue [28, 29].

Many studies have shown MTR to be a very strong indicator of tissue damage. However, this damage may not specifically be a change in myelination. For example myelinic and inter-axonal nerve components have been shown to present similar steady-state MTR characteristics [30].

1.1.5 Myelin Development

Yakovlev and Lecours reported from a post mortem study in 1967 that while most areas of the brain myelinate in the first postnatal year certain regions, such as the corpus callosum, reticular formation and frontal lobes, continue to develop the myelin sheath into

adolescence [31]. In addition the forebrain was show to continue to myelinate into adulthood. Further histopathological work was performed by Benes *et al* [32] which supported Yakovlev and Lecours' findings although this study limited its investigations solely to the hippocampus.

Even though histopathological studies would be considered to be the closest to a "gold standard" in the field of quantification of myelin, the paucity of post-mortem brains within this critical age range which do not exhibit disease or traumatic injury means that it is difficult to verify findings using this method. We are required to utilise a non-invasive technique to continue the study of myelin development. Since computerised tomography scans deliver a dose of radiation to the region being imaged MR is the only completely non-invasive technique which allows the subjects to be investigated.

One may find in the literature a large number of MR studies which strongly illustrated the myelin development in neonates, infants and children and in recent years there has been a growing number which illustrate this development continuing, in certain regions, into adolescence and adulthood [33-36]. Studies which investigate the trace and fractional anisotropy of a diffusion tensor have also shown a relationship with age using a variety of methods: voxel-based morphometry [11, 26], region of interest analysis [37, 38] and most recently, tractography [39]. Volumetric studies have shown an increase in white matter volume accompanied by a decrease in grey matter volume with age [40-43] and studies of cortical thickness show a thinning of most regions throughout childhood and adolescence implying an increase in myelination [44-46].

These studies have supported the age related changes in white matter structure, specifically supporting a continuation of myelination into adolescence but with different time patterns for different regions of the brain. A growing body of research is providing evidence that myelin development is correlated with cognitive function, be that general intelligence [47], reading ability [48-51] or visual spatial information processing [34]. The goal of this thesis is to provide evidence to support this hypothesis by correlating the subjects' intelligence quotient (IQ) scores with the amount of myelin water in their corpus callosum. This relationship has never been previously shown with T_2 relaxation.

The studies referenced above have primarily used conventional and diffusion tensor imaging. These methods are therefore subject to the limitations discussed in section 3.2, that is, the non-specificity to myelin which is inherent in the DTI technique. This thesis introduces a novel analysis method to investigate the normal myelination of children aged 8 to 12 and demonstrates, for the first time, quantitative T_2 relaxation in children. This method is described in chapter 3.

1.1.6 Specific Hypotheses

With the information presented in this chapter in mind, we can return to the criteria listed at the beginning of this chapter and now see how myelination of neuronal axons fulfils the requirements as a biological model of development of mental functions. First, myelination of the axon will increase the intensity and frequency of cell firing, both of which are classically associated with learning. Second, the brain myelinates in a regional and

sequential pattern and the majority of this myelination occurs during the first two decades of life. Thirdly, Yakovlev and Lecours [31] and Benes *et al* [32] showed from their histological studies that structures associated with specific abilities are in the process of myelinating when these abilities are typically acquired.

Finally, the fourth of the criteria stated above requires that rates of maturation should vary across individuals. As discussed earlier, previous studies have shown a correlation with age [33-36]. However, these studies which controlled for age have shown that cognitive ability alone is correlated to myelination. Indeed, age is simply a proxy measure of maturity and should not be a perfect definer of myelin development. For this study children were chosen from a very narrow age range in order to remove, as much as possible, the relationship between myelin density and age. Therefore we were able to investigate the relationship between cognitive ability without the overwhelming influence of the confounding factor of age.

The Wechsler Intelligence Scale was developed based on the philosophy that intelligence is "the global capacity to act purposefully, to think rationally, and to deal effectively with [one's] environment" [52]. In this study we use the Wechsler Intelligence Scale for Children – Revised (WISC-R) as our measure of cognitive ability. The test comprises a battery of 10 subtests which are compiled to provide verbal, performance and full intelligence quotients. These scores are age corrected but do not account for any other factor which may affect the child's cognitive development. It is generally recognised as the most robust behavioural measure of overall cognitive ability.

The corpus callosum is a region which connects the two hemispheres of the brain and its development allows faster and more effective communication between the two hemispheres. Children's response times, which are improved by myelination of axons in the developing brain, have been shown to correlated with traditional IQ measures [53]. In addition, it has a large cross sectional area and is highly oriented and therefore can be unambiguously identified in the sagittal plane.

The specific hypothesis of this thesis is that the MWF of the children's corpus callosum will be correlated with their IQ measures, and to a lesser extent, their age. In this study a novel voxel based analysis method is introduced and it is hypothesised that this analysis will yield more specific results than the region of interest method regarding the relationship between the myelin and cognitive measures. This study aims to provide evidence for an age-independent measure of development, namely the level of myelin development as measured by quantitative T_2 MRI.

2 Physics of Nuclear Magnetic Resonance and Principles of Magnetic Resonance Imaging

2.1.1 The NMR Signal: Precession of a non-zero magnetic dipole in a magnetic field

Nuclear magnetic resonance (NMR) was first described in 1938 by Isidor Rabi and in 1952 Bloch and Purcell were awarded the Nobel Prize in physics for their work refining the technique. The first biological images were created in the 1970s, in the 1980s MRI became clinically prevalent, and the following decade brought the introduction of functional MRI to indentify brain activity. Today the International Society for Magnetic Resonance in Medicine has over 5,000 members and presents 4,000 new pieces of work every year at their annual meeting.

This section outlines the physics behind this outstanding, elegant and extremely influential method of non-invasive biological imaging. It assumes an upper undergraduate level knowledge of quantum mechanics.

2.1.2 The Intrinsic Nuclear Spin and Magnetic Moment

An atom consists of protons, neutrons and electrons. The protons and neutrons are situated in the nucleus of the atom while the electrons occupy orbitals outside of the nucleus. The energy levels which these fermions occupy are filled according to two rules: one, the Pauli Exclusion Principle, which states that no electron can occupy the same energy state; and two, the Aufbau Principle, which dictates that each electron occupies the

lowest available energy state. For NMR we are interested in the nucleons: the protons and neutrons.

Three quantum numbers are used to characterise the state of a nucleon: the orbital angular momentum, *l*, the spin angular momentum, *s*, and the total angular momentum, **j**. The total angular momentum of the nucleus is the nuclear spin, **I**, defined as the vector sum of the angular momentum of each nucleon. The most energetically stable state is achieved when nucleons are paired such that their spin and orbital angular momenta sum to zero. Therefore when a nucleus has an even number of nucleons its nuclear spin is always zero.

The magnetic dipole moment, **μ**, of the nucleus is directly proportional to the nuclear spin, **I**, with a constant of proportionality defined as the gyromagnetic ratio, γ.

$$\boldsymbol{\mu} = \gamma \boldsymbol{I} \qquad \textbf{Equation 2-1}$$

If a nucleus has a non-zero nuclear spin, which can only occur if there are either unpaired protons or unpaired neutrons or both, a non-zero net magnetic dipole moment will be observed. Nucleons with angular momentum and a non-zero magnetic dipole moment are said to posses the nuclear magnetic resonance property and are generally referred to as "spins".

In biological experiments carbon-13, oxygen-17, fluorine-19, sodium-23 and phosphorus-31 all have the NMR property and are studied but it is hydrogen with its one proton (nuclear spin = ½) which contributes most of the signal from biological tissue. An average

human, weighing 150 lbs, has approximately 5 x 10^{27} hydrogen protons in water, fat and organic molecules. Unless the signal from hydrogen in water is suppressed (as in MR spectroscopy) the signal from other non-zero dipoles is negligible. For simplicity, this chapter will only consider the signal from hydrogen from here on.

In the absence of a strong magnetic field the spins will be randomly oriented, as shown in figure 2-1(A) and no overall magnetisation will be discerned. However, when a strong external magnetic field is present the non-zero magnetic dipole moments will interact with it and cause the spins to either align with or against the magnetic field. These are the spin-up and spin-down orientations and are shown in figure 2-1(B).

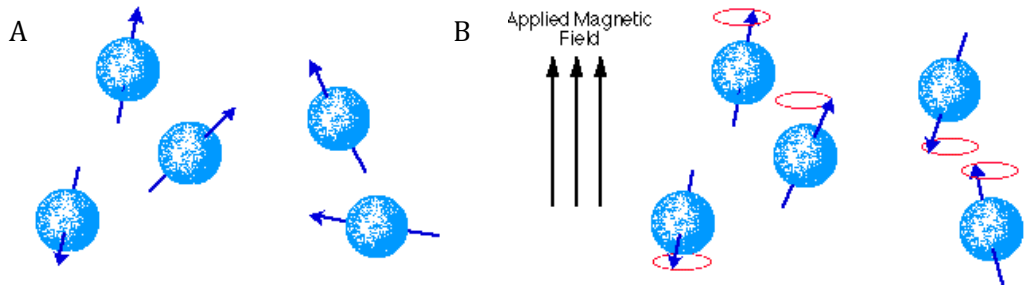

Figure 2-1: Spins in free space with random orientations (A) and in an external magnetic field (B)

The difference between the number of spins in each state is the macroscopic magnetic moment, or net magnetisation, **M.**

2.1.3 The Macroscopic Magnetic Moment

The energy of the interaction between a magnetic dipole moment, **μ**, and an external magnetic field, **B**, is their dot product and is known as the Zeeman energy.

$$E = -\boldsymbol{\mu} \cdot \boldsymbol{B} \qquad \textbf{Equation 2-2}$$

The Hamiltonian operator for the system can be defined by combing equations 2-1 and 2-2:

$$H = -\hbar\gamma \boldsymbol{B} \cdot \boldsymbol{I} \qquad \textbf{Equation 2-3}$$

If the direction of **B** is defined to be along the z-axis, $\boldsymbol{B} = B\hat{\boldsymbol{z}}$, then it is only the component of the magnetic dipole moment in the z direction, μ_z which is non-zero. In this case the Hamiltonian operator reduces to

$$H = -\hbar\gamma B_z I_z \qquad \textbf{Equation 2-4}$$

Using the Schrödinger equation the energy of the eigenstate, where m_s is the projection of the spin onto the z-axis, is given by:

$$\begin{aligned} H\left|m_s\right\rangle &= E\left|m_s\right\rangle \\ -\hbar\gamma B_z I_z\left|m_s\right\rangle &= -\hbar\gamma B_z m_s\left|m_s\right\rangle \\ E &= -\hbar\gamma B_z m_s \end{aligned} \qquad \textbf{Equation 2-5}$$

For hydrogen, or any nucleus whose nuclear spin is ±½, there are two possible values for the energy, either $E^- = -\hbar\gamma B/2$ which corresponds to the spin-up orientation ($s = +½$), or the slightly higher $E^+ = \hbar\gamma B/2$ which corresponds to the spin-down orientation ($s = -½$). The separation of the nucleus' ground state into these two orientations after the application of an external magnetic field is called Zeeman splitting and is illustrated in figure 2-2. The difference in energy between the two states is $\Delta E = \hbar\gamma B$. Note the dependence on the external magnetic field strength. The higher the field the easier it is to detect the net magnetisation.

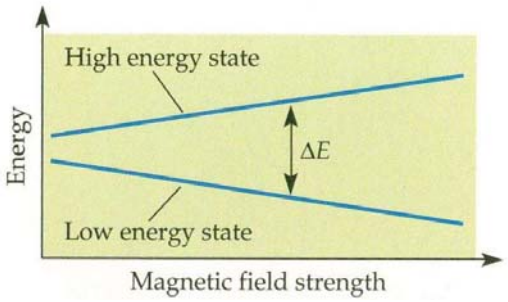

Figure 2-2: The Zeeman Effect. The energy difference between the high energy (up) and low energy (down) states increases with the external magnetic field strength [54].

Using the Boltzmann distribution (equation 2-6) to calculate the probability of a proton occupying either of the two energy states (when a large number of protons are involved) leads to the ratio of the number of protons in the spin-up state (N^-) to the number in the spin-down state (N^+) (equation 2-7).

$$P(E) = Ce^{-E/kT} \qquad \textbf{Equation 2-6}$$

C is a constant of the system, k is the Boltzmann constant and T is the temperature measured in Kelvin

$$R = \frac{N^-}{N^+} = \frac{P(E^-)}{P(E^+)} = \frac{Ce^{-E^-/kT}}{Ce^{-E^+/kT}} = e^{\Delta E/kT} = e^{\hbar\gamma B/kT} \qquad \textbf{Equation 2-7}$$

At an average room temperature of 300K and a typical clinical magnetic field strength of 1.5T the ratio of the number of protons in the spin-up state to those in the spin-down state is approximately $1.00000163 \times 10^{-6}$ which means that for every two million protons there will be three which has overcome thermal randomisation and has aligned themselves in the direction of the applied magnetic field, settling in the spin-up state rather than in the spin-down state.

We are now able to calculate the net magnetisation, or macroscopic magnetic moment, for a particular temperature:

$$\boldsymbol{M_0} = \boldsymbol{\mu}\left(N^- - N^+\right) = \boldsymbol{\mu}\left(N^- + N^+\right)\frac{\left(N^- - N^+\right)}{\left(N^- + N^+\right)}$$

$$= \boldsymbol{\mu}N\frac{(R-1)}{(R+1)} = \boldsymbol{\mu}N\frac{\left(e^{\Delta E/kT} - 1\right)}{\left(e^{\Delta E/kT} + 1\right)} = \boldsymbol{\mu}N\tanh\left(\Delta E/2kT\right) \qquad \textbf{Equation 2-8}$$

This value M_0 is called the thermal equilibrium value of the magnetisation.

2.1.4 Equation of motion of M: Precession in a Magnetic Field

In 1897 Joseph Larmor found that if an aligning force is applied to a spinning object it will undergo precession. Therefore, if a spinning object is tipped away from the aligning force it will precess about the axis of the force. In this section we will define the equation of motion of the net magnetisation as it moves in an external magnetic field.

As illustrated in figure 2-3, the motion of a magnetic moment in a magnetic field is analogous to movement of a spinning top, with the magnetic field exerting the aligning force instead of a gravitational field.

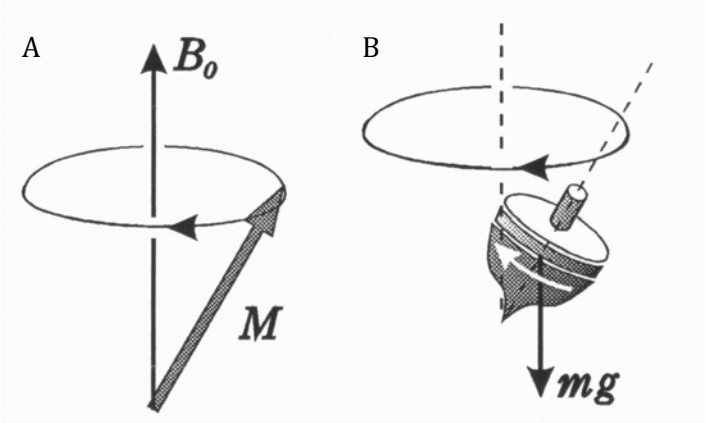

Figure 2-3: Precession. (A) The movement of the net magnetisation, M, around the applied magnetic field is analogous to (B) a spinning top in an external gravitational field [55].

Classical mechanics states that the rate of change of the total angular momentum, **I**, equals the total torque, **T**, exerted on the system:

$$\frac{d\boldsymbol{I}}{dt} = \boldsymbol{T} \qquad \textbf{Equation 2-9}$$

For a system made up of many nuclei in a unit volume under a magnetic field, **B**, the total torque is the cross product between the total magnetic moment, **M**, and the magnetic field, as defined by the system's electrodynamics:

$$\boldsymbol{T} = \boldsymbol{M} \times \boldsymbol{B} \qquad \textbf{Equation 2-10}$$

The gyromagnetic ratio (introduced in equation 2-1) is the ratio of the total angular momentum to the magnetic moment. This definition holds for the macroscopic properties of the system and therefore equations 2-9 and 2-10 can be combined to provide the equation of motion of M:

$$\frac{d\boldsymbol{M}}{dt} = \gamma \boldsymbol{M} \times \boldsymbol{B} \qquad \textbf{Equation 2-11}$$

This relationship holds true whether the magnetic field is time dependent or not.

This equation of motion of the macroscopic magnetisation if it is deviated from the direction of the external magnetic field can either be derived using classical mechanics, as shown here, or quantum mechanics and both investigations yield the same result, which is that the magnetisation will precess around the axis of the external magnetic field. There are situations in which the behaviour of the hydrogen nuclei requires a quantum mechanical approach, such as NMR spectroscopy, but these situations are outside the scope of this thesis and hence I have not outlined the quantum mechanical proof here.

2.1.5 Relaxation of the NMR Signal: The Bloch Equation

The equation of motion derived in section 2.1.3 describes the motion of the magnetic moment under the assumption that there are no other interfering factors and implies that the perturbed magnetisation vector would precess indefinitely about the axis of the applied magnetic field. In reality, the interactions between individual nuclei and the interactions between each nucleus and its surroundings result in an exchange of energy which acts to restore the thermal equilibrium magnetisation (equation 2-8). The return of the macroscopic magnetic moment to thermal equilibrium is known as relaxation.

The effect of the interaction of the spin of a nucleus with its surroundings (spin-lattice interaction) is that the nucleus transfers energy to these surroundings and therefore loses energy itself. The spin-spin interaction is the interaction of the spin of a nucleus with that

of another nucleus and the effect of this interaction is the dephasing of these spins, causing a decrease in the net magnetisation.

In 1946 Bloch introduced a detailed phenomenological relationship which aimed to model these energy exchanges, defining the equation of motion of **M** in terms of its components, M_x, M_y and M_z, along three orthogonal axes with unit vectors $\hat{\boldsymbol{x}}$, $\hat{\boldsymbol{y}}$ and $\hat{\boldsymbol{z}}$ [56]:

$$\frac{d\boldsymbol{M}}{dt} = \gamma \boldsymbol{M} \times \boldsymbol{B} - \frac{M_x \hat{\boldsymbol{x}} + M_y \hat{\boldsymbol{y}}}{T_2} - \frac{\left(M_z - M_0\right)\hat{\boldsymbol{z}}}{T_1} \qquad \textbf{Equation 2-12}$$

The Bloch equation (equation 2-12) uses simple exponential processes to model the spin-lattice and spin-spin interactions. The spin-lattice interactions cause the net magnetisation to relax along the direction of the magnetic field while the spin-spin interactions cause the relaxation of the net magnetisation perpendicular to the direction of the magnetic field. The terms T_1 and T_2 are used to describe the spin-lattice, or longitudinal, and spin-spin, or transverse, relaxation times respectively.

By separating the Bloch equation into its components along each axis it can be solved to give three general solutions:

$$\begin{aligned} M_x(t) &= \left[M_x(0)\cos(\omega_0 t) + M_y(0)\sin(\omega_0 t)\right] e^{-t/T_2} \\ M_y(t) &= \left[-M_x(0)\sin(\omega_0 t) + M_y(0)\cos(\omega_0 t)\right] e^{-t/T_2} \\ M_z(t) &= M_0 + \left[M_z - M_0\right] e^{-t/T_1} \end{aligned} \qquad \textbf{Equation 2-13}$$

Figure 2.4(a) illustrates the time development of each of these three components and figure 2.4(b) allows the three-dimensional motion of the magnetisation vector to be envisaged.

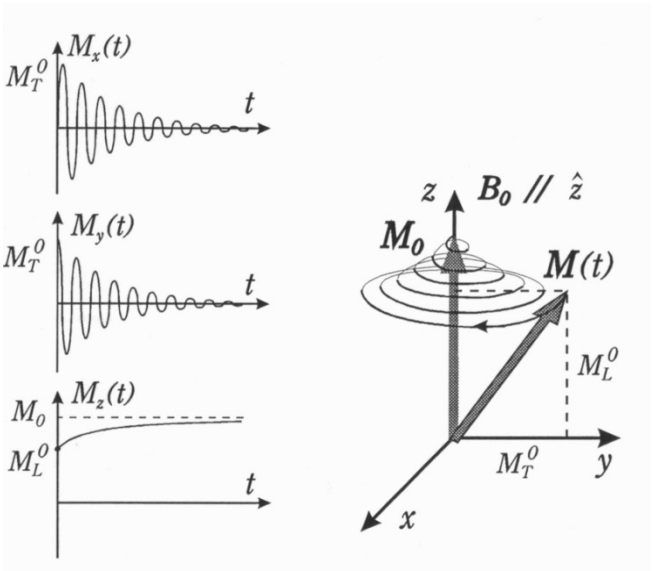

Figure 2-4: Time evolution of the magnetisation vector M. (A) M_x, M_y and M_z as functions of time. (B) The motion of M vector in 3D. The M vector undergoes a Larmor precession as well as T_1 and T_2 relaxations to finish at the equilibrium state M_0 [55].

The longitudinal component of **M** is M_z since the magnetic field is defined as being aligned along the z-axis. The transverse component can be defined as a single complex variable M_T and expressed as:

$$M_T \equiv M_x + iM_y$$
$$M_T(t) = M_T(0)e^{-t/T_2}e^{i\omega_0 t} \qquad \textbf{Equation 2-14}$$

When the relaxation effects are negligible, for example during short time periods such as RF excitation and signal detection (as addressed in section 2.2), equation 2-15 will yield the

same solution as the solutions to the Bloch equation when the relaxation times are replaced with infinity.

2.1.6 Detection of the NMR Signal

2.1.7 The rotating frame of reference

The precession described in section 2.1.3 will be observed for any and every nucleus which has a magnetic dipole moment and the frequency of the precession will be characteristic of the element. This frequency is commonly known as the Larmor frequency, in honour of the Irish physicist whose work described the dynamics of precessing systems.

If the movement of the magnetisation vector is observed from a stationary frame of reference then its motion as it relaxes is very complicated. However, if a rotating frame of reference is utilised, and specifically one which is rotating at the Larmor frequency, we are able to easily observe only the motion of the vector which is caused by the transverse and longitudinal relaxation.

An effective magnetic field, $\mathbf{B_{eff}}$, is introduced, and defined as

$$\boldsymbol{B}_{eff} = \boldsymbol{B} + \frac{\boldsymbol{\omega}}{\gamma} \qquad \textbf{Equation 2-15}$$

where $\boldsymbol{\omega}$ is the frequency of the rotating frame. This allows the equation of motion excluding the effects of relaxation as defined in equation 2.11, to be transformed from the stationary frame (x, y, z) into the rotating frame (x', y', z'):

$$\frac{d\boldsymbol{M}}{dt} = \boldsymbol{M} \times \left(\gamma \boldsymbol{B} + \boldsymbol{\omega} \right) = \gamma \boldsymbol{M} \times \boldsymbol{B}_{eff} \qquad \textbf{Equation 2-16}$$

If $\mathbf{B_{eff}}$ is defined to equal zero then the motion of **M**, excluding effects of relaxation, in the rotating frame, will also be zero. Therefore the angular frequency of the rotating frame is defined to be:

$$\boldsymbol{\omega} = -\gamma B \hat{z} \qquad \textbf{Equation 2-17}$$

2.1.8 RF Excitation

The precession described thus far describes the motion of the net magnetisation when perturbed from its equilibrium position, $\mathbf{M_0}$. This perturbation is achieved by applying a magnetic field pulse for a short time, orthogonally to the static magnetic field, $\mathbf{B_0}$. Since it is necessary to transform the pulse into the rotating frame of reference described in section 2.2.1, it must oscillate in the stationary frame of reference in order that the magnetisation vector is pushed in the same direction at each rotation.

The frequency of the oscillations is the Larmor frequency, **ω**, for the element being studied. This frequency is in the radio frequency (RF) range for conventional MRI and therefore this pulse is commonly referred to as the RF pulse. If this pulse does not oscillate at the Larmor frequency it will not affect the magnetisation vector much since in the rotating frame it will not appear to be a constant field. A pulse of this nature is termed to be "off-resonance" and will take longer to tip the longitudinal magnetisation away from the axis of the B_0 field due to the inefficient trajectory caused by an incorrect pulse frequency.

The RF pulse is analogous to pushing a child on a swing. The most efficient push is at the top of her swing and has the same frequency as the child's motion. An off-resonance pulse is equivalent to pushing the child too soon, or too late.

While in the stationary frame of reference the applied magnetic field ($\mathbf{B_1}$) is oscillating at the Larmor frequency, in the rotating frame of reference it is a constant field along an axis perpendicular to the $\hat{z}$ axis. For this explanation this axis is set to be the $\hat{x}'$ axis. Note that the $\hat{z}$ and $\hat{z}'$ axes are the same, although the former refers to the axis in the laboratory frame, and the latter to the rotating frame, because the rotating frame revolves around the axis of the $\mathbf{B_0}$ field. This notation extends to the transverse axes.

The only magnetic field affecting **M** is $B_1\hat{x}'$ since the effective magnetic field is B_1 in this frame of reference. Therefore, the magnetisation vector will now rotate around this magnetic field and will be perturbed from the $\hat{z}'$ direction to trace a circle orthogonal to the $\hat{x}'$ axis as shown in figure 2-5.

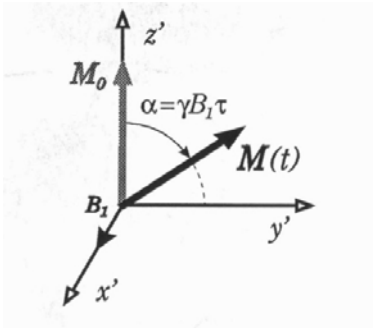

Figure 2-5: The M vector precesses about the effective magnetic field in the rotating frame [55].

The angle though which M will turn (α) depends on how long the $\mathbf{B_1}$ field is applied for and can be calculated, $\alpha = \gamma B_1 \tau$. Since τ is small (a few ms) for a flip angle of π radians, it is reasonable to ignore the effects of relaxation during the application of the RF pulse.

2.1.9 Induction Signal Detection

According to Faraday's law, a charged particle moving in a magnetic field will induce a voltage in an orthogonally orientated coil. In this case an induction coil is oriented perpendicular to the $\hat{\boldsymbol{x}}$ axis and the magnitude of the induced voltage is

$$V = \frac{1}{c}\frac{d\Phi}{dt} \qquad \textbf{Equation 2-18}$$

where c is the speed of light and Φ is the total magnetic flux in the coil which is proportional to the component of the magnetisation along the $\hat{\boldsymbol{x}}$ axis.

As discussed in section 2.1.4 the transverse component of the magnetisation is modelled to relax back to $\mathbf{M_0}$, exponentially. The coil is in the stationary frame of reference and the induced voltage will therefore oscillate at the Larmor frequency, reflecting the angular frequency of the rotating frame of reference. Figure 2-6 illustrates this oscillating exponential decay. This oscillating voltage creates an alternating (at the Larmor frequency) current which is detected by the electronics of the RF receiver and provides the signal we use to create a magnetic resonance image. Image reconstruction is described in section 2.4.

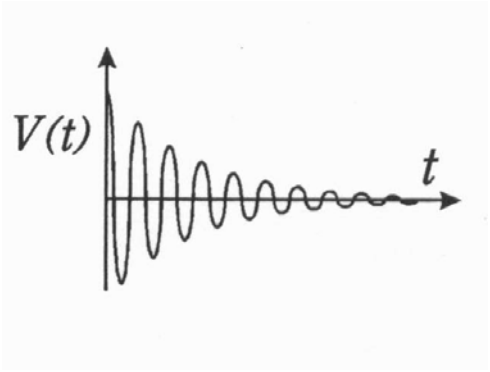

Figure 2-6: Induction signal detection [55].

2.1.10 Spin Echo Experiments: T_2 measurement

2.1.11 Spin Dephasing

In section 2.2.2 it was noted that if the RF pulse does not oscillate at the Larmor frequency it will not affect the magnetisation vector much since in the rotating frame the effective magnetic field generated by this pulse will not appear to be a constant field. In a similar manner any variations in the magnitude or direction of the main magnetic field, $\mathbf{B_0}$, across a region will cause the nucleons across the region to each experience slightly different magnetic fields and $\mathbf{B_{eff}}$ will not be defined to be exactly zero. As the spins precess they will therefore move at different rates.

The gradual accumulation of spins which are precessing slower or faster than the theoretical Larmor frequency lead to a macroscopic magnetic moment of zero, since the transverse components of each of the individual nucleon's magnetic moments eventually return to their original random orientation within the x-y plane (the spins are still tilting

towards the z axis as they undergo longitudinal relaxation). Therefore, due to this process of spin dephasing, no signal is detected. Figure 2-7 illustrates the dispersion of the transverse components of the individual spins.

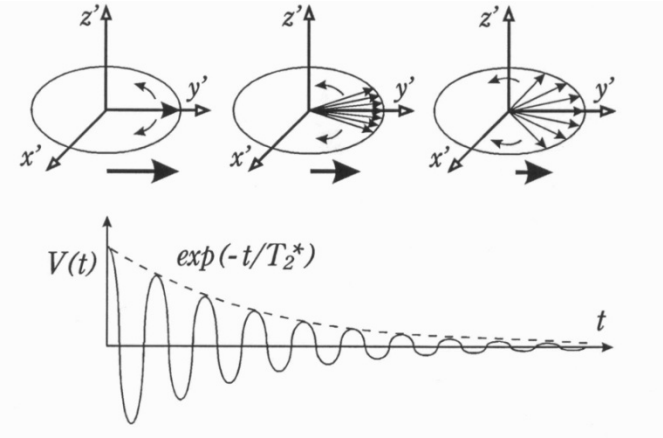

Figure 2-7: Spin dephasing due to magnetic field inhomogeneities in the transverse plane over time [55]. Below is the time course of the NMR signal.

The time taken for this signal to decay to 1/e is T_2*. It is not the transverse relaxation time T_2 but is related by taking into account the field inhomogeneities, ΔB:

$$\frac{1}{T_2^*} = \frac{1}{T_2} + \gamma \Delta B \qquad \textbf{Equation 2-19}$$

2.1.12 The CPMG Spin Echo Sequence: True T_2 Measurement

Imagine if the spin dephasing discussed above could be reversed. This would allow the field inhomogeneities to be compensated for and the measurement of the true transverse relaxation time. The Carr, Purcell, Meiboom and Gill (CPMG) pulse sequence, developed in 1958, does exactly that [57].

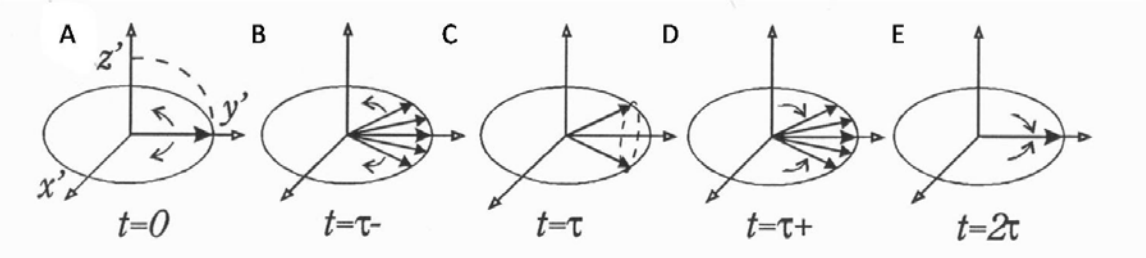

Figure 2-8: Rotating frame spin phase diagram for a CMPG spin-echo experiment. At time τ the second RF pulse rotates the spins 180° along the y' axis. At time 2τ the spins are rephased [55].

The spin phase diagram for the CMPG sequence is shown in Figure 2-10. Figures 2-10(A) and 2-10(B) illustrate the dephasing of the spins after being flipped into the transverse plane after a 90° x' pulse.

At time τ, another RF pulse rotates the spins 180° along the y' axis (figure 2-8(C)). The individual magnetic moments continue to change according to their particular equation of motion, with some precessing faster than the rotating frame and others rotating more slowly, but now they are moving in the opposite direction (figure 2-8(D)). Therefore, after time 2τ (measured from the original RF excitation of the nuclei), the spins are rephased back into alignment (figure 2-8(E)).

These 180° pulses are called refocusing pulses and can be repeated at times 3τ, 5τ, 7τ etc to allow spins to be rephrased over a long time period. This leads to the accurate calculation of the true T_2 relaxation time since the dephasing effect of the interactions between nuclei is not recoverable and will cumulate as illustrated below in figure 2-9.

Equation 2-20 relates the signal after n refocusing pulses, S(2nτ), to the original signal strength, S(0), and T_2.

$$S(2n\tau) = S(0)e^{\frac{-2n\tau}{T_2}} \qquad \textbf{Equation 2-20}$$

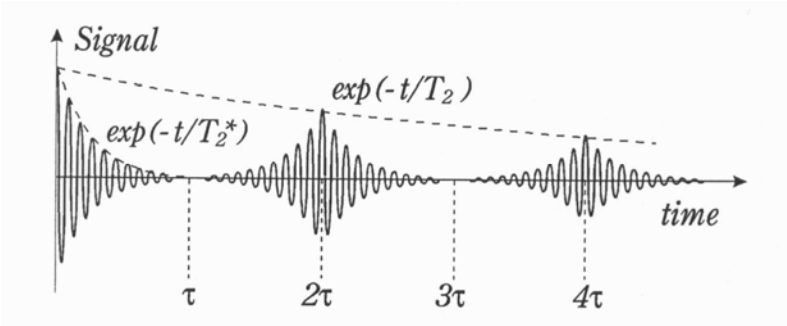

Figure 2-9: Induction signals as a train of spin echoes [55].

The original spin-echo sequence created by Carr and Purcell was similar to the CPMG sequence and the only difference between them is that in the CP sequence the 180° pulse was aligned along the x' axis rather than the y' axis [58]. In this sequence errors in the flip angle initiated by the RF pulse would cumulate at each subsequent refocusing pulse. The CPMG sequence refocuses these errors at every second echo at the same time as refocusing the spins themselves.

2.1.13 Spatial Localisation

Investigating the precession characteristics of each individual spin (i.e. their frequency and phase) when a known spatial dependence is introduced to the applied magnetic field allows an MR image to be created. Three techniques are utilised to achieve the information

required to reconstruct the image in 3 dimensions: slice selection, frequency encoding and phase encoding.

Although in the following explanation the x, y and z axes are used to represent the three orthogonal directions in which the data is encoded, it is important to remember that these are not the only possible orientations. One of the MRI technique's greatest assets is the fact that these axes can be rotated in any direction allowing images to be acquired in any oblique plane.

Slice Selection

A z dependence on the spin precession frequency can be introduced using a magnetic field which changes linearly along the z axis. The gradient of this field, i.e., its rate of change, is G_z and alters the magnetic field in the z direction to:

$$B = \left(B_0 + zG_z \right) \qquad \textbf{Equation 2-21}$$

which in turn adjusts the spin precession frequency to:

$$\omega(z) = \gamma \left(B_0 + zG_z \right) \qquad \textbf{Equation 2-22}$$

It is not desirable to have a slice which is too thin because it would take too many repetitions to image a volume in the body. Therefore a range of frequencies are required. The band width of the RF pulse, $\Delta\omega$ is related to the thickness of the slice, d, by $d = \frac{\Delta\omega}{\gamma G}$.

In order to excite a rectangular slice the RF pulse cannot maintain a constant amplitude since that would excite a sinc shaped slice. However, to a first order approximation the temporal modulation of the amplitude is related to its frequency spectrum by a Fourier transform. To achieve a rectangular slice in the time domain, a sinc shaped RF pulse is required, as shown in figure 2-12.

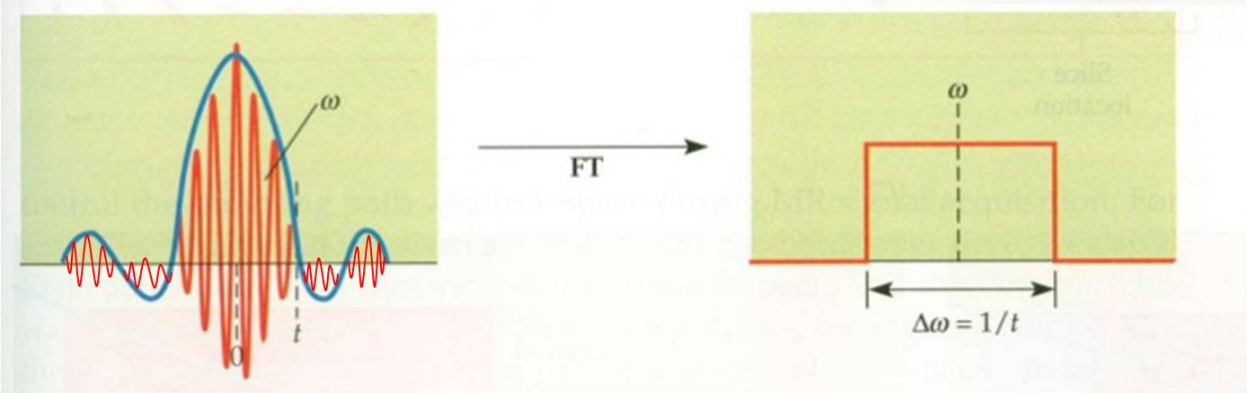

Figure 2-10: A sinc shaped slice selection pulse represents a rectangular distribution of excited frequencies [54].

Slice location and thickness are determined by three factors: the centre frequency of the excitation pulse (ω), the bandwidth of the excitation field (Δω) and the strength of the gradient field (G_z). The centre frequency and the gradient field determine the slice location and the bandwidth and the gradient field determine the slice thickness. Theoretically we could simply slide the centre frequency up and down and acquire data from a variety of slices. However, due to off-resonance excitation just beyond the edges of the slices, in most scans the slices are acquired in an interleaved fashion: for example for an acquisition of ten slices the sequence would acquire the first, third, fifth, seventh and ninth before going back to acquire the second, fourth, sixth, eighth and tenth slices in order to minimise any problems from overlapping slices.

Frequency Encoding

Following slice selection a second gradient, G_x, may be applied along the x axis so that different nuclei precess at different frequencies according to their position along the x axis. This spatial dependence will be observed in the signal received by the induction coil. If the relaxation effects are ignored during the G_x application, which is reasonable since the gradient is only applied for a short amount of time, the magnetisation can be modelled as described in equation 2-14 and thus the complex signal received, in terms of the spin density distribution along the axis, P(x), can be written as:

$$C(t) = \int P(x) e^{i\gamma x G_x t} dx \qquad \textbf{Equation 2-23}$$

Using a substitution of $k=\gamma G_x t$ and an inverse Fourier transform, the x coordinates of the excited spins, P(x), can be recovered from the signal received:

$$S(k) = \int_{-\infty}^{\infty} P(x) e^{ikx} dx$$
$$P(x) = \frac{1}{2\pi} \int_{-\infty}^{\infty} S(k) e^{-ikx} dx \qquad \textbf{Equation 2-24}$$

Phase Encoding

The encoding in the third and final orthogonal direction is generated using another gradient, this time along the y axis. In fact, it is necessary to apply a variety of gradients. A gradient is applied for a short amount of time before the frequency encoding gradient, changing the phase of the magnetisation vector. Once the sequence has been repeated for a

range of gradients, both positive and negative, a vector encoding the phase of each voxel is created:

$$e^{i\gamma y G_y t}$$

Equation 2-25

A Fast Fourier Transform is then used to extract the y position of the voxel.

In this section we have shown how slice selection and frequency and phase encoding techniques are used to determine the magnetisation within each individual voxel and thus create two-dimensional maps of the scanned region. There are many more ways to acquire data. For example, given the right slice prescription, phase encoding can readily be extended to three directions, replacing the slice selection pulse, and providing increased signal-to-noise ratio and superior spatial resolution.

2.1.14 T_2 relaxation analysis

A multi echo CPMG sequence can reverse the signal loss due to the dephasing of the transverse magnetisation caused by inhomogeneities in different water environments and allow the calculation of the true T_2 of a sample as described in section 2.3.2. The resulting decay curve includes the contribution from protons in each environment and therefore encodes information concerning the number and relative size of each environment. This section summarises the techniques required for this process.

It is conceptually very easy to understand that an in vivo MR image would represent protons constrained within different water environments and therefore that the true T_2 of a sample would follow a multi-exponential decay pattern as those protons with short T_2 ceased their contribution to the decay earlier than those with more free space around them. Figure 2-11 shows the difference between a mono-exponential T_2 decay (that of free water) and a multi-exponential decay from CNS tissue. It is clear therefore that the model used to approximate true T_2 decay must be multi-exponential, although we do not initially know how many water reservoirs will contribute to it.

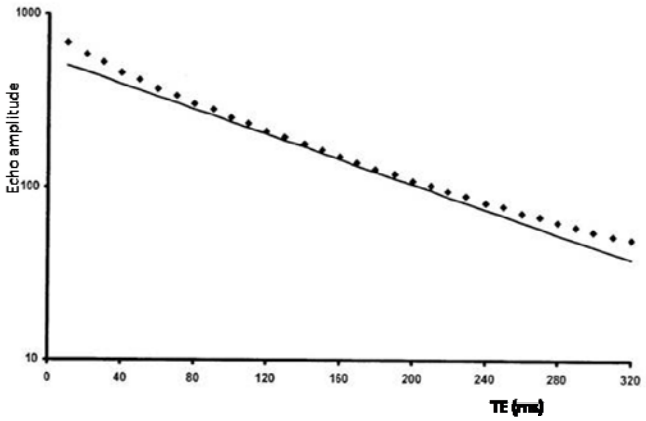

Figure 2-11: Monoexponential T_2 decay curve from water (solid line) and multiexponential decay curve from CNS white matter (dots) [59].

The general integral equation describing multi-exponential T_2 relaxation (equation 2-26) describes N data points, y_i, measured at times t_i. $S(T_2)$ is the amplitude distribution of the contributing exponentials as a function of their characteristic relaxation time.

$$y(t_i) = y_i = \int_a^b s(T_2) e^{-\frac{t_i}{T_2}} dT_2 \quad i = 1, 2 \ldots N \qquad \textbf{Equation 2-26}$$

Linear techniques overcome the necessary shortcoming of nonlinear techniques in that they do not require any a priori assumptions as to the number of contributing exponentials. Instead, they assume a large number of T_{2j} times and solve for the corresponding amplitudes, allowing for the fact that some may be zero. These techniques are guaranteed to converge to the absolute minimum within the defined solution space.

The utilisation of a convergence algorithm to compute the T_2 times requires the discretisation of $s(T_2)$ in equation 2-26. Equation 2-27 illustrates this discretisation through the assumption that the distribution is a sum of M delta functions with areas s_j and known relaxation times T_j.

$$s(T_2) = \sum_{j=1}^{M} s_j \delta\left(T_2 - T_{2_j}\right) \qquad \textbf{Equation 2-27}$$

The general form of the linear system of equations is shown in equation 2-28 and it is this system we wish to solve.

$$y_i = \sum_{j=1}^{N} A_{ij} s_j \quad i = 1, 2 \ldots N \qquad \textbf{Equation 2-28}$$

The chi squared statistic (equation 2-29) represents the misfit of the acquired data, y_i, to the value predicted by the constructed model, y_i^p due to noise in the acquired data.

$$\chi^2 = \sum_{i=1}^{N} \frac{\left(y_i^p - y_i\right)^2}{\sigma_i^2} \qquad \textbf{Equation 2-29}$$

The nonnegative least squares (NNLS) algorithm approach to solving equation 2-28 involves finding the set of s_j which minimises the least squares misfit (equation 2-30) which, when normalised to unit variance, also minimises the χ^2 misfit.

$$\sum_{i=1}^{N}\left|\sum_{j=1}^{M}A_{ij}s_j - y_i\right|^2 \qquad \textbf{Equation 2-30}$$

In reality it is unlikely that a biological sample of central nervous system tissue will exhibit a distribution of T_2 values which are perfectly described by the discrete solution offered by the minimisation of equation 2-30. An adaptation which introduces additional constraints regularising the solutions can be used and is illustrated in equation 2-31. Here μ is the trade-off parameter and the **H** matrix contains the additional constraints on the data, such as that of solution curvature. The minimisation of equation 2-31 leads to T_2 distributions which more accurately reflect the physical characteristics of biological tissue environments.

$$\sum_{i=1}^{N}\left|\sum_{j=1}^{M}A_{ij}s_j - y_i\right|^2 + \mu\sum_{k=1}^{K}\left|\sum_{j=1}^{M}H_{kj}s_j\right|^2 \qquad \textbf{Equation 2-31}$$

2.1.15 NNLS Signal to Noise Ratio

The quality of any image increases with increased signal to noise ratio (SNR) due to the reduced influence from noise in the image. SNR usually compares the signal from the protons within a volume to the background noise. The parameter SNR_{NNLS} is conceptually analogous to SNR and provides a quantitative measure of "goodness of fit".

SNR_{NNLS} compares the signal density with the χ^2 misfit described in equation 2-30. This measure illustrates how well the data has been fitted to the multi-exponential T_2 distribution modelled using the NNLS algorithm described above. Small values of the χ^2 misfit would represent a good fit to the data, while large values imply a poor model for the data. Therefore, as with SNR, a large value of SNR_{NNLS} is desirable.

$$SNR_{NNLS} = \frac{Signal\ Density}{\chi^2}$$ **Equation 2-32**

It is necessary to consider the signal density when quantifying "goodness of fit" since a voxel with small signal density will produce a less reliable model than those with higher signal due to the fewer available data points.

This is a novel measure which has not previously been utilised in T_2 analysis. One of the aims of this thesis was to investigate the applications of this measure and these are discussed in detail in later chapters.

3 Method

This chapter outlines the novel voxel-based method utilised in the investigations undertaken along with details of MR scan acquisition and data analysis. The hypotheses tested are outlined in the final section of this chapter.

3.1.1 Specifically Imaging the Development of Myelin: A Novel Voxel Based Analysis

The average myelin water fraction, as described above, which takes the signal from a whole ROI, has the benefit of high signal to noise (SNR). However, it also homogenises the region, meaning that an area with low myelin development may present with the same average MWF as an area with advanced myelin development containing regions of water with longer T_2. Therefore, an analysis method which allows the areas within an ROI which have high myelin content to be detected, even if they are surrounded by regions with low myelin content, is required to further probe the ROI.

An individual voxel has the benefit of having identical dimensions for all subjects and all scans. In our technique the structure of interest is still outlined with a conventional ROI but it is the voxels which it prescribes that are considered for analysis.

The voxels are then classified as highly myelinated voxels (HMVs) if their MWF above a certain critical value. Since the voxels have much lower SNR than the overall ROI the actual calculated voxel MWF is not included in the analysis past the binary consideration of

whether or not it is classified as an HMV. In this study, the first to use this technique, a variety of critical values are investigated.

A strong benefit to this voxel based investigation is that it allows for variations in the size of the structure between subjects. The average MWF by definition loses this information and presents only the density of myelin within the region. The voxel based analysis proposed in this thesis does not simply investigate density of myelin but the overall quantity of myelin within the structure.

3.1.2 Data Acquisition

3.1.3 Subjects

Eight normal male children aged between 9 and 12 years were chosen for this study (average age: 131 months, range: 114 – 144 months). They satisfied the recruitment criteria of normal school progress and a clear medical history including no psychiatric conditions.

3.1.4 MR Acquisition

MR images were acquired using a 1.5T GE scanner operating at the 5.7 software level in a single slice acquisition in the midsagittal plane. T_2 relaxation data was acquired using a single slice modified 32-echo Carr-Purcell-Meiboom-Gill sequence [7]. Crusher gradients were included to eliminate the signal from tissue outside the selected slice [60]. The

repetition time was 3 s, echo spacing = 10 ms, slice thickness = 5 mm, field of view = 22 cm and a 256 x 128 matrix was created. Each voxel measured 0.86mm x 0.86mm x 5mm.

Scans were examined by a trained radiologist for unacceptable artefacts. Specifically, due to the extended data acquisition time of the T_2 relaxation sequence, scans with motion artefact (3) were corrupted by motion artefact and were excluded from the analysis.

3.1.5 Data Analysis

The 32-echo decay curves were decomposed into an unspecified number of exponential components using a regularised non-negative least squares algorithm [61]. The myelin water fraction was defined as the fraction of the T_2 signal between 10 and 50ms relative to the total T_2 signal. Regions of interest (ROIs) were drawn around the corpus callosum on the first echo of the CPMG sequence, which has high in-plane anatomic resolution.

The average MWF was calculated using the entire signal from the ROI and a myelin water map, illustrating the MWF for each voxel within an ROI, was created by carrying out a NNLS analysis of the signal from each individual voxel.

SNR_{NNLS} Filter

Maps were created which illustrated the SNR_{NNLS} for each voxel as defined by the ratio of the TE = 0 amplitude of the fitted decay curve to the standard deviation of the residuals of the fitted T_2 decay curve. These maps were used to extricate reliable myelin water fraction

results from T_2 relaxation data. This operation was required since the sagittally acquired T_2 data was noisy in some regions due to the presence of CSF flow in the interhemispheric fissure.

A variety of potential minimum SNR_{NNLS} values were investigated to determine the sensitivity to the minimum SNR_{NNLS} value of the outcome of the results. Minimum SNR_{NNLS} values tested ranged from 90 to 110 in unit increments. These values were chosen from visual analysis of the SNR_{NNLS} maps by an observer trained in brain anatomy. SNR_{NNLS} values greater than 110 yielded myelin maps which excluded major white matter tracts and values lower than 90 included voxels in regions containing cerebrospinal fluid.

A filtered myelin water map was subsequently created which excluded voxels with SNR_{NNLS} less than the minimum value. This is a novel approach to T_2 analysis which has not been employed previously.

Voxel Based Analysis

The voxel based analysis of MWF proposed for the first time in this thesis counts the number of voxels within the corpus callosum with a MWF greater than a critical MWF value and designated these "highly myelinated voxels". 15 different critical values evenly spaced from 0.01 to 0.15 ($HMV_{0.01}$ to $HMW_{0.15}$) were investigated for both filtered and unfiltered myelin maps.

3.1.6 Cognitive Measures

A trained investigator conducted the ten subtests of the WISC-R and recorded the scores. The Verbal IQ, Performance IQ and Full IQ were calculated from the age corrected and population normalised subtest scores in the standard fashion.

3.1.7 Statistical Analysis

The cognitive scores were regressed using the Pearson's Product Moment against the various myelin measures and significance was determined using a two-tailed test at $p = 0.01$ level. In addition the filtered myelin water maps were ranked by eye by three informed judges according to the amount of myelin within the corpus callosum. The judges were blinded to any subject details and were provided by a colour bar indicating the MWF values represented by each colour.

4 Results

4.1.1 Maps

Figure 4-1 is an example of one subject's (a) raw myelin map, (b) SNR_{NNLS} map, (c) a filtered myelin map, which excludes all voxels with SNR_{NNLS} less than 100 and (d) filtered myelin map masked to solely illustrate the corpus callosum, superimposed on the first echo of the T_2 relaxation sequence. The inset for (d) shows a close up of the corpus callosum.

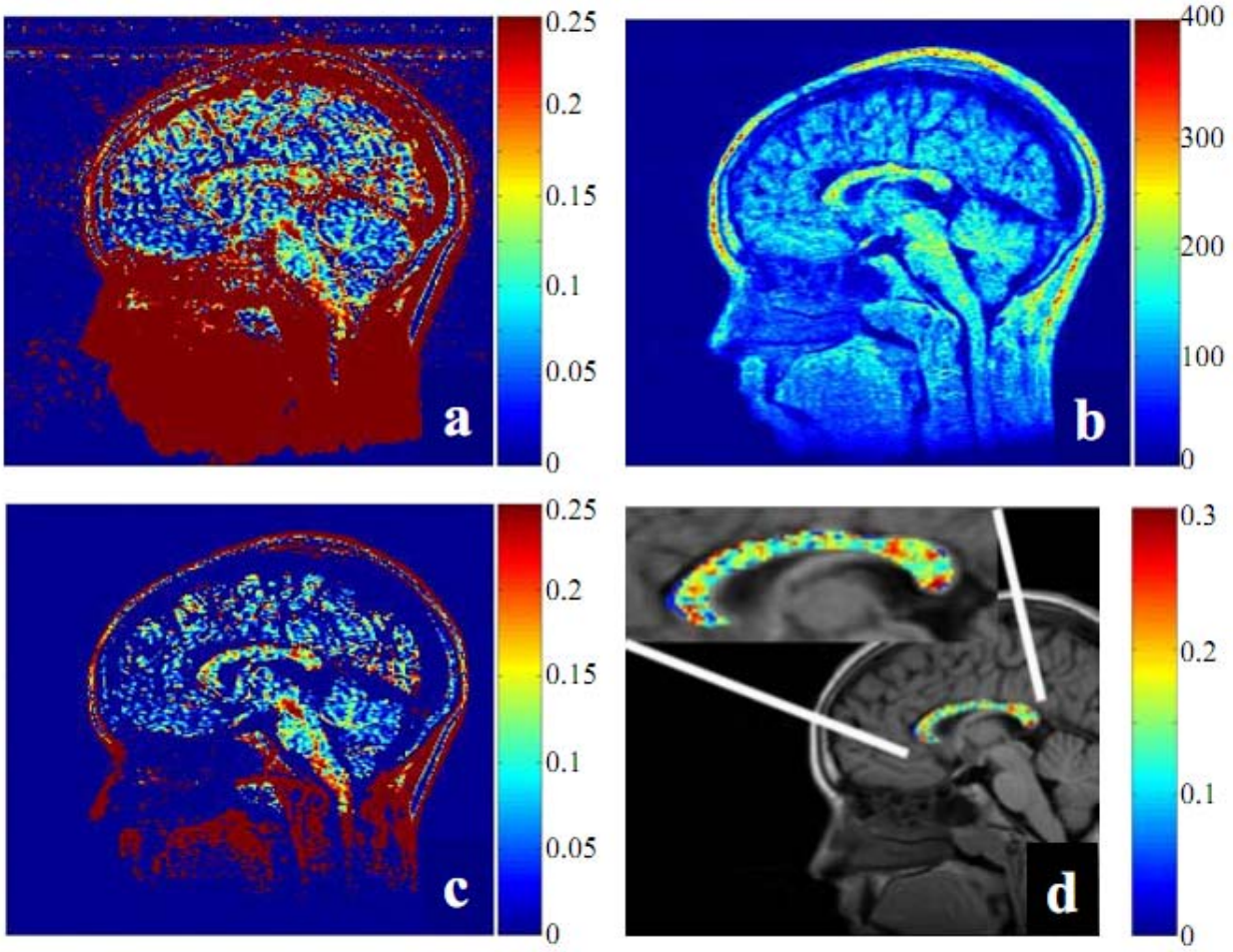

Figure 4-1 One subject's (a) raw myelin water map, (b) SNR_{NNLS} map, (c) filtered myelin water map (created by excluding all voxels with SNR_{NNLS} less than 100) and (d) myelin water map of the corpus callosum superimposed on the first echo of the CMPG sequence. Note that the colour bars represent different values for the different types of maps; in (a), (c) and (d) the colour represents the MWF and in (b) the colour represents the SNR_{NNLS}. Excluded voxels were given the value -0.01.

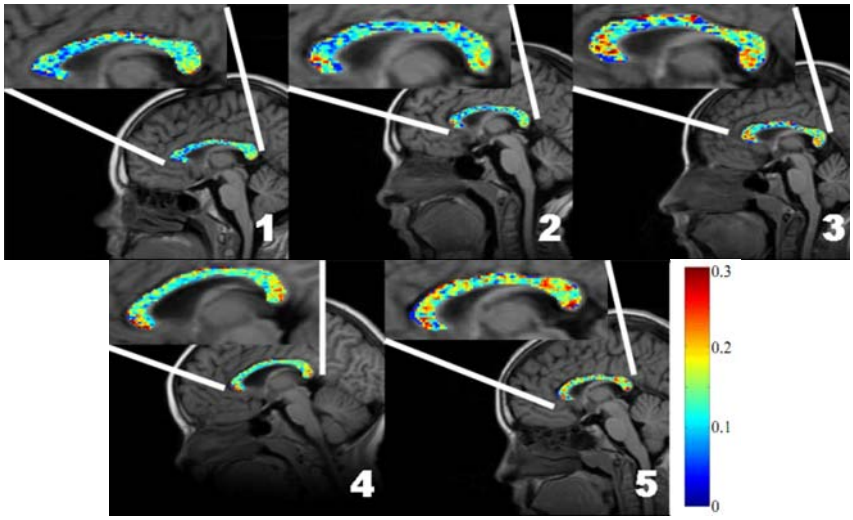

Figure 4-2 Myelin water maps of the corpus callosum superimposed on the first echo of the CPMG sequence for all 5 subjects. The colour bar represents the MWF of each voxel within the ROI prescribing the corpus callosum. This region is shown in clearer detail inset in the picture. These maps have all been filtered to exclude voxels with SNR_{NNLS} less than 100 and are presented in their unanimous ranking by three blinded judges

Figure 4-2 presents the filtered myelin map, masked to solely illustrate the corpus callosum, superimposed on the first echo of the T_2 relaxation sequence for each subject. The inset shows a close up of the corpus callosum. The maps were ranked by eye, in order of least to most myelinated. This ranking was unanimous between 3 blinded judges and perfectly correlated with the average MWF for each ROI. The Spearman's rank correlation coefficient for this ranking with age was 0.825 but not statistically significant.

4.1.2 SNR_{NNLS} Filter

Figure 4-3 demonstrates the finding that within the range of minimum SNR_{NNLS} values investigated, a robust and nearly constant correlation between the voxel myelin measures and verbal IQ (which were the only statistically significant correlations) was observed for

certain HMV critical values between minimum values of 90 and 100. At minimum values above 100 the correlations began to be more varied. This outcome was probably due to the exclusion of too many voxels, leading to results which are more likely to be influenced by noise. On this basis, a SNR_{NNLS} minimum value of 100 was chosen to maximise the number of true highly myelinated voxels while still removing those which did not sufficiently fit the model.

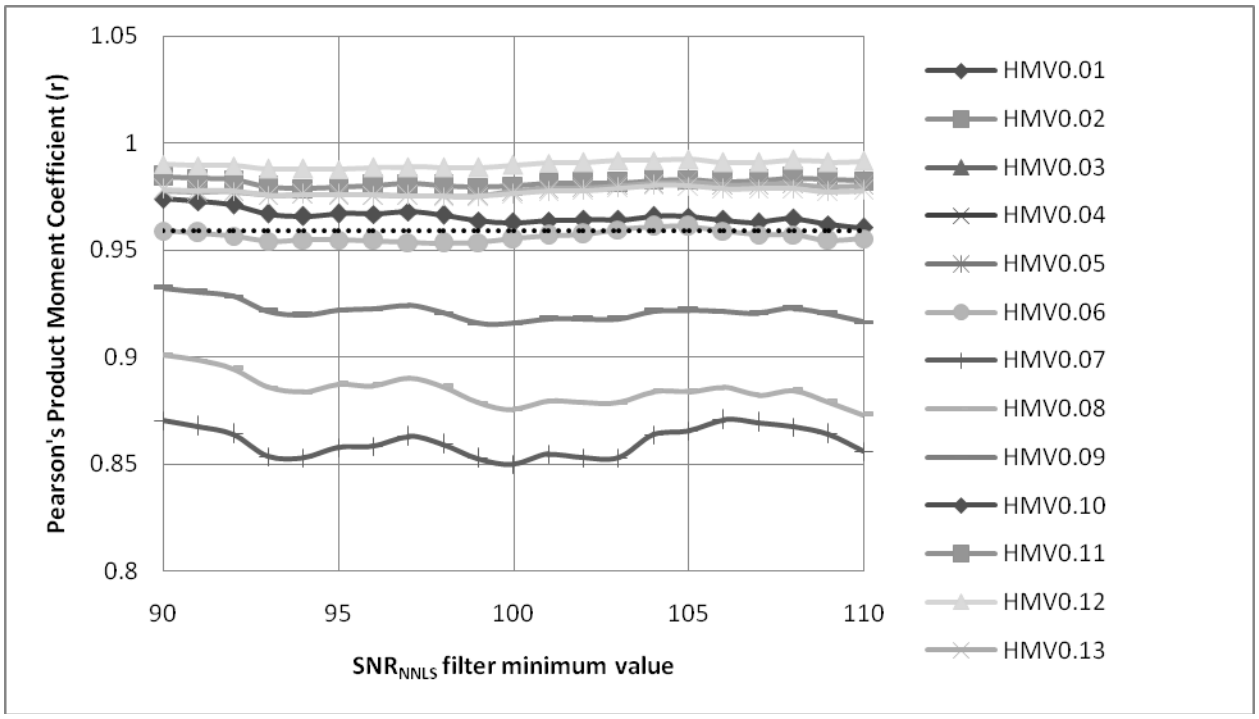

Figure 4-3 Pearson's Product Moment correlation coefficient between voxel based myelin measures and VIQ for SNR_{NNLS} filter minimum values (90-110). The plot clearly shows a highly uniform and robust correlation for significant correlations (r>0.847). Noise began to affect the correlation coefficients at SNR_{NNLS} filter values above 100 and therefore a SNR_{NNLS} filter minimum value of 100 was chosen to maximise the number of true highly myelinated voxels included in the analysis while still removing voxels with low SNR_{NNLS} which did not fit well to the data.

4.1.3 Voxel Based Analysis

Figure 4-4 illustrates the different critical points for the voxel based myelin measures. The correlation increased as the HMV critical points were increased. The correlations were not significant for critical points higher than 0.14 ($p < 0.01$) which is reasonable: within the smallest ROI the number of voxels with MWF greater than 0.15 constituted only 12% of its total size. It is reasonable to expect that the paucity of voxels with adequate SNR_{NNLS} and very high MWF will prevent significant correlations since at that point too many "highly myelinated voxels" will be excluded from the measure and the results will more closely resemble noise.

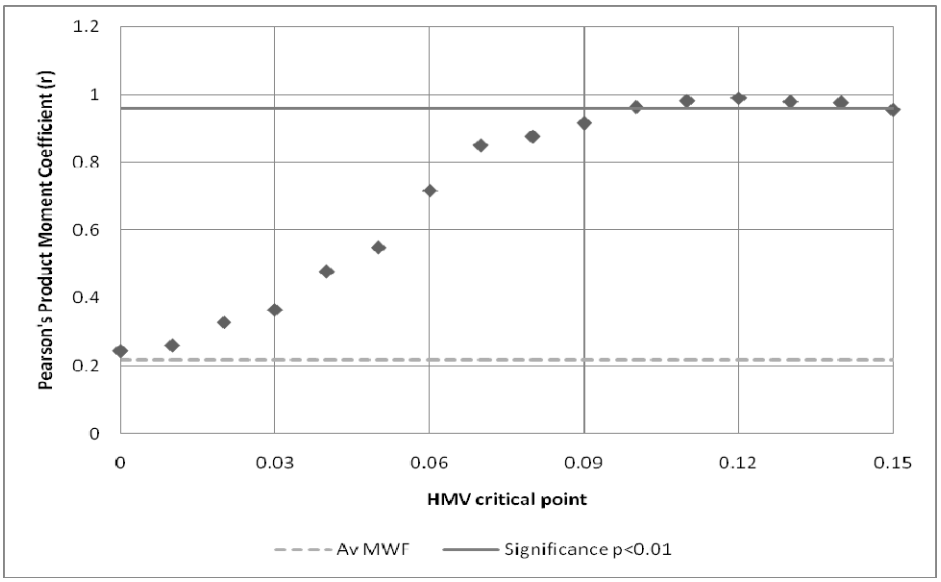

Figure 4-4 Pearson's Product Moment coefficient for correlations between filtered (voxels with SNR_{NNLS} < 100 excluded) myelin measures of various critical points. As the voxels with low coefficients are excluded from the analysis the correlations become stronger peaking at a maximum correlation of 0.990 for a critical point of 0.12. The correlation of average MWF with VIQ is shown as a dotted line at r = 0.217.

The highest correlation between any of the myelin water measures was found for filtered $HMV_{0.12}$ which represents the number of voxels with SNR_{NNLS} above 100 and MWF greater

than 0.12. These highly myelinated voxels represented on average 40% of the total ROI (range: 29% - 53%). $HMV_{0.12}$ correlated almost perfectly with verbal IQ: r = 0.990, p = 0.001 (figure 4-5).

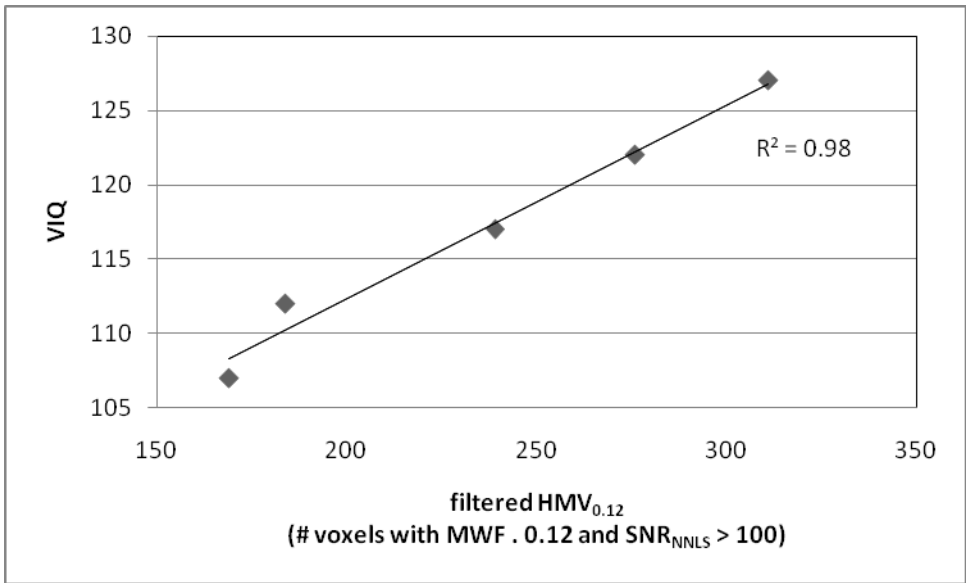

Figure 4-5 Correlations between VIQ and filtered $HMV_{0.12}$ which represents the number of voxels with MWF > 0.12 and SNR_{NNLS} > 100.

4.1.4 Non-significant Correlations

There were no significant correlations between any of the myelin water measures and subject age. The average MWF did not correlate with the voxel based myelin water measures. No myelin water measures correlated with performance or full IQ measures and average MWF did not correlate with verbal IQ. In addition all the IQ measures were independent of age (as designed in the WISC-R test).

5 Discussion

The results of this study have provided evidence for a non-invasive method of quantifying development in preadolescent children. Where the average MWF is unable to provide a significant correlation with cognitive measures of global intelligence this novel voxel-based method illuminates a convincing correlation with verbal IQ. Our results support other studies which have also shown this relationship between cognitive ability and myelin development [34, 47-51].

That the correlation with this global IQ measure came from investigating the corpus callosum is not surprising. This structure acts to communicate between the two hemispheres and therefore is entirely necessary for the completion of complex tasks, such as those required in the verbal section of the WISC-R. The lack of significant correlations between performance IQ and the myelin water measures may be explained by different demands from the sub-tests of this measure: these tasks may not rely on cross-hemispheric communication as heavily as those recruiting language abilities and therefore a link between the performance IQ score and the myelin measures would not been seen. This in turn would explain the lack of correlation with full IQ as it is a linear sum of verbal and performance IQ scores.

It is worth noting that, while the sample size is very small, the chosen significance was conservative and the resulting probability is corrected for sample size. Therefore we can be confident in our results. Clearly, a larger sample size is required to draw firm

conclusions about the correlation between cognitive measures and level of myelination. In interpreting the results one should not suggest that there is an almost perfect linear correlation between VIQ and the voxel based myelin measures over a larger population, rather that since these measures are able to describe a significant correlation in a very small sample further investigations into this relationship can be confidently prepared.

The SNR_{NNLS} filter succeeded in removing the impossibly high myelin water fractions represented in cerebrospinal fluid (CSF) and the sinuses in sagittal myelin water maps. The CSF contains proton spins which may be moving quickly out of the excitation slice and hence artefactually showed a short T_2, and the sinuses comprise mostly air and therefore also showed a short T_2 due to magnetic susceptibility artefact. Since neither fit the NNLS model of multi-exponential decay their SNR_{NNLS} was sufficiently low that they were excluded from analysis when the filter was applied. There are still some erroneously high MWF values included on the filtered map, in the skull and neck for example. These regions are affected by B_0 and B_1 field inhomogeneities. However, the difference between the filtered and unfiltered myelin water maps in figure 4-1 is striking: the overall resolution of the image is vastly increased and the myelinated white matter of the brain can be easily distinguished.

While the average MWF ROI approach previously used in myelin water investigations provides better signal to noise ratios, it also blinds the observer to some potentially important details of the structure under investigation. For example, both the heterogeneity within the ROI and the size of the ROI are not reported when an average density is

provided. Our voxel-based method can better illuminate the properties of admixtures and regions of different sizes. In addition, this approach can be used in techniques other than MRI, for example, in the investigation of binding compounds in Positron Emission Tomography.

The binary system of simply counting the number of voxels with MWF greater than a critical value allows the problem of low SNR within each individual voxel to be addressed. While the critical value of 0.12 may seem arbitrary, the correlation between HMV0.12 and VIQ demonstrates the highly plausible result that on average 40% of voxels within a highly oriented white matter structure, such as the corpus callosum, can be considered to be highly myelinated.

That the average MWF did not correlate significantly with any of the HMV measures highlights the fact that we are obtaining different information from the two methods and provides support that the voxel-based method can provide more information than the average MWF alone. This measure of myelin density across the ROI should not to be excluded from future analyses. It correlated perfectly with the trained judges rankings of myelin development (figure 4-2). The two analysis techniques together support and complement each other.

By only selecting subjects from a narrow age range we were successful in eliminating age as a significant effect in our results. As previous work has shown, age is an important factor in development but it is not able to account for individual variation alone.

6 Conclusion and Future Directions

The specific aims of this study were to find a technique which used MRI to quantify a biologically relevant measure of cognitive development without the confounding factor of age, and to investigate this relationship using the new MR method. The non-invasive quantitative measure of myelin using T_2 relaxation which has been demonstrated in this thesis allowed the relationship between cognitive ability and myelin development to be investigated. The SNR_{NNLS} filter and voxel-based analysis method have elucidated a strong correlation between the amount of myelin within the corpus callosum and verbal IQ and the narrow age range of our subjects has allowed correlations to be reasonably independent of age.

This study was the first to quantify myelin water in children. The usual difficulty scanning young subjects apply: they move. Three of the subjects had to be removed from the analysis due to excess motion artefact and it is likely that all the scans had some corruption from motion. Training the subjects, for example in mock scanning machines which provide feedback when they move, may help to preserve data in future studies.

In addition, this method suffers from the long acquisition time which limits the technique to one slice. Further work by Kolind and Mädler, presented in 2008 [62] and supporting previous work [18] will not only allow 3D imaging, which permits much better delineation of regions of interest, but also faster imaging, which may also help remove movement artefact. This advance in pulse programming will allow other regions of white matter to be

investigated, such as the fronto-parietal white matter which has been implicated in other studies [63]. The application of this technique at MRI machines of 3T would be of interest, since the greater signal to noise may illuminate even more subtle changes in white matter maturation.

As always, longitudinal studies are always desirable in developmental studies. The individual differences which are seen in this study, due to the narrow age range, may continue further into development. Additional measures of cognitive function, such as measures of working memory (for example the WISC-R digit span subtest) or fluid reasoning (using Raven's Progressive Matrices) would further this work into the imaging of the development of specific types of cognitive ability. A comparison of diffusion tensor imaging and this quantitative T_2 technique in identical subject populations will allow direct comparison of the results described in this thesis with work already existing in the literature.

Finally, as previously mentioned, this study only looked at a small sample of children. Clearly larger groups are necessary to provide data which can be extrapolated to the general population. However, with even with the small group size, this thesis has succeeded in presenting a novel, biologically relevant, non-invasive method for imaging the development of human children and adolescents as they continue to myelinate critical structures for those cognitive abilities which make us human. Namely, the novel voxel based approach of analysis the myelin water fraction as calculated using T_2 relaxation.

7 Bibliography

1. Adleman, N.E., et al., *A Developmental fMRI Study of the Stroop Color-Word Task.* NeuroImage, 2002. **16**(1): p. 61.
2. Helmuth, L., *Neuroscience. Glia tell neurons to build synapses.* Science (New York, N.Y.), 2001. **291**(5504): p. 569.
3. Reed, T.E., P.A. Vernon, and A.M. Johnson, *Sex difference in brain nerve conduction velocity in normal humans.* Neuropsychologia, 2004. **42**(12): p. 1709.
4. Tsuda, M., K. Inoue, and M.W. Salter, *Neuropathic pain and spinal microglia: a big problem from molecules in "small" glia.* Trends in neurosciences, 2005. **28**(2): p. 101.
5. Tsuda, M., et al., *P2X4 receptors induced in spinal microglia gate tactile allodynia after nerve injury.* Nature, 2003. **424**(6950): p. 778.
6. Ullian, E.M., et al., *Control of synapse number by glia.* Science (New York, N.Y.), 2001. **291**(5504): p. 657.
7. MacKay, A., et al., *In vivo visualization of myelin water in brain by magnetic resonance.* Magnetic resonance in medicine : official journal of the Society of Magnetic Resonance in Medicine / Society of Magnetic Resonance in Medicine, 1994. **31**(6): p. 673.
8. Menon, R.S., M.S. Rusinko, and P.S. Allen, *Proton relaxation studies of water compartmentalization in a model neurological system.* Magnetic resonance in medicine : official journal of the Society of Magnetic Resonance in Medicine / Society of Magnetic Resonance in Medicine, 1992. **28**(2): p. 264.
9. Laule, C., et al., *Myelin water imaging of multiple sclerosis at 7 T: Correlations with histopathology.* NeuroImage, 2008.
10. Laule, C., et al., *Myelin water imaging in multiple sclerosis: quantitative correlations with histopathology.* Multiple sclerosis (Houndmills, Basingstoke, England), 2006. **12**(6): p. 747.
11. Barnea-Goraly, N., et al., *White matter development during childhood and adolescence: a cross-sectional diffusion tensor imaging study.* Cerebral cortex (New York, N.Y.: 1991), 2005. **15**(12): p. 1848.
12. Stewart, W.A., et al., *Spin-spin relaxation in experimental allergic encephalomyelitis. Analysis of CPMG data using a non-linear least squares method and linear inverse theory.* Magnetic resonance in medicine : official journal of the Society of Magnetic Resonance in Medicine / Society of Magnetic Resonance in Medicine, 1993. **29**(6): p. 767.
13. Vasilescu, V., et al., *Water compartments in the myelinated nerve. III. Pulsed NMR results.* Experientia, 1978. **34**(11): p. 1443.
14. Webb, S., et al., *Is multicomponent T2 a good measure of myelin content in peripheral nerve?* Magn Reson Med, 2003. **49**(4): p. 638.
15. Beaulieu, C., F.R. Fenrich, and P.S. Allen, *Multicomponent water proton transverse relaxation and T2-discriminated water diffusion in myelinated and nonmyelinated nerve.* Magnetic resonance imaging, 1998. **16**(10): p. 1201.

16. Oh, J., et al., *Measurement of in vivo multi-component T2 relaxation times for brain tissue using multi-slice T2 prep at 1.5 and 3 T.* Magnetic resonance imaging, 2006. **24**(1): p. 33.
17. Oh, J., et al., *Measurement of in vivo multi-component T2 relaxation times for brain tissue using multi-slice T2 prep at 1.5 and 3 T.* Magn Reson Imaging., 2006. **24**(1): p. 33-43. Epub 2005 Dec 19.
18. Maedler, B. and A.L. MacKay, *In-vivo 3D Multi-component T2-Relaxation Measurements for Quantitative Myelin Imaging at 3T.* 14th Annual Meeting of the International Society of Magnetic Resonance in Medicine, 2006.
19. Matsumae, M., et al., *Distribution of intracellular and extracellular water molecules in developing rat's midbrain: comparison with fraction of multicomponent T(2) relaxation time and morphological findings from electron microscopic imaging.* Child's nervous system : ChNS : official journal of the International Society for Pediatric Neurosurgery, 2003. **19**(2): p. 91.
20. Kuker, W., et al., *Modern MRI tools for the characterization of acute demyelinating lesions: value of chemical shift and diffusion-weighted imaging.* Neuroradiology, 2004. **46**(6): p. 421.
21. Filippi, C.G., et al., *Developmental delay in children: assessment with proton MR spectroscopy.* AJNR.American journal of neuroradiology, 2002. **23**(5): p. 882.
22. Kreis, R., T. Ernst, and B.D. Ross, *Development of the human brain: in vivo quantification of metabolite and water content with proton magnetic resonance spectroscopy.* Magnetic resonance in medicine : official journal of the Society of Magnetic Resonance in Medicine / Society of Magnetic Resonance in Medicine, 1993. **30**(4): p. 424.
23. Song, S.K., et al., *Diffusion tensor imaging detects and differentiates axon and myelin degeneration in mouse optic nerve after retinal ischemia.* NeuroImage, 2003. **20**(3): p. 1714.
24. Song, S.K., et al., *Dysmyelination revealed through MRI as increased radial (but unchanged axial) diffusion of water.* NeuroImage, 2002. **17**(3): p. 1429.
25. Beaulieu, C., *The basis of anisotropic water diffusion in the nervous system - a technical review.* NMR in biomedicine, 2002. **15**(7-8): p. 435.
26. Schmithorst, V.J., et al., *Correlation of white matter diffusivity and anisotropy with age during childhood and adolescence: a cross-sectional diffusion-tensor MR imaging study.* Radiology, 2002. **222**(1): p. 212.
27. Wolff, S.D. and R.S. Balaban, *Magnetization transfer contrast (MTC) and tissue water proton relaxation in vivo.* Magnetic resonance in medicine : official journal of the Society of Magnetic Resonance in Medicine / Society of Magnetic Resonance in Medicine, 1989. **10**(1): p. 135.
28. Ropele, S., et al., *A comparison of magnetization transfer ratio, magnetization transfer rate, and the native relaxation time of water protons related to relapsing-remitting multiple sclerosis.* AJNR.American journal of neuroradiology, 2000. **21**(10): p. 1885.
29. Sled, J.G., et al., *Regional variations in normal brain shown by quantitative magnetization transfer imaging.* Magnetic resonance in medicine : official journal of the Society of Magnetic Resonance in Medicine / Society of Magnetic Resonance in Medicine, 2004. **51**(2): p. 299.

30. Does, M.D., et al., *Multi-component T1 relaxation and magnetisation transfer in peripheral nerve.* Magnetic resonance imaging, 1998. **16**(9): p. 1033.
31. Yakovlev, P.I. and A.R. Lecours, *The myelogenetic cycles of regional maturation of the brain.* Regional development of the brain in early life, 1967: p. 3â€“70.
32. Benes, F.M., et al., *Myelination of a key relay zone in the hippocampal formation occurs in the human brain during childhood, adolescence, and adulthood.* Archives of General Psychiatry, 1994. **51**(6): p. 477.
33. Liston, C., et al., *Frontostriatal microstructure modulates efficient recruitment of cognitive control.* Cerebral cortex (New York, N.Y.: 1991), 2006. **16**(4): p. 553.
34. Mabbott, D.J., et al., *White matter growth as a mechanism of cognitive development in children.* NeuroImage, 2006. **33**(3): p. 936.
35. Nagy, Z., H. Westerberg, and T. Klingberg, *Maturation of White Matter is Associated with the Development of Cognitive Functions during Childhood.* Journal of cognitive neuroscience, 2004. **16**(7): p. 1227.
36. Olesen, P.J., et al., *Combined analysis of DTI and fMRI data reveals a joint maturation of white and grey matter in a fronto-parietal network.* Cognitive Brain Research, 2003. **18**(1): p. 48.
37. Schneiderman, J.S., et al., *Diffusion Tensor Anisotropy in Adolescents and Adults.* Neuropsychobiology, 2007. **55**: p. 96.
38. Snook, L., et al., *Diffusion tensor imaging of neurodevelopment in children and young adults.* NeuroImage, 2005. **26**(4): p. 1164.
39. Kanaan, R.A., et al., *Tract-specific anisotropy measurements in diffusion tensor imaging.* Psychiatry research, 2006. **146**(1): p. 73.
40. Giedd, J.N., et al., *Brain development during childhood and adolescence: a longitudinal MRI study.* Nature neuroscience, 1999. **2**: p. 861.
41. Jernigan, T.L. and P. Tallal, *Late childhood changes in brain morphology observable with MRI.* Developmental medicine and child neurology, 1990. **32**(5): p. 379.
42. Jernigan, T.L., et al., *Maturation of human cerebrum observed in vivo during adolescence.* Brain : a journal of neurology, 1991. **114 (Pt 5)**(Pt 5): p. 2037.
43. Reiss, A., et al., *Brain development, gender and IQ in children: A volumetric imaging study.* Brain, 1996. **119**(5): p. 1763.
44. Shaw, P., et al., *Intellectual ability and cortical development in children and adolescents.* Nature, 2006. **440**(7084): p. 676.
45. Sowell, E.R., et al., *Mapping cortical change across the human life span.* Nature neuroscience, 2003. **6**(3): p. 309.
46. Sowell, E.R., et al., *Longitudinal mapping of cortical thickness and brain growth in normal children.* The Journal of neuroscience : the official journal of the Society for Neuroscience, 2004. **24**(38): p. 8223.
47. Schmithorst, V.J., et al., *Cognitive functions correlate with white matter architecture in a normal pediatric population: a diffusion tensor MRI study.* Human brain mapping, 2005. **26**(2): p. 139.
48. Beaulieu, C., et al., *Imaging brain connectivity in children with diverse reading ability.* NeuroImage, 2005. **25**(4): p. 1266.
49. Deutsch, G.K., et al., *Children's reading performance is correlated with white matter structure measured by diffusion tensor imaging.* Cortex; a journal devoted to the study of the nervous system and behavior, 2005. **41**(3): p. 354.

50. Klingberg, T., et al., *Microstructure of Temporo-Parietal White Matter as a Basis for Reading Ability Evidence from Diffusion Tensor Magnetic Resonance Imaging.* Neuron, 2000. **25**(2): p. 493.
51. Niogi, S.N. and B.D. McCandliss, *Left lateralized white matter microstructure accounts for individual differences in reading ability and disability.* Neuropsychologia, 2006. **44**(11): p. 2178.
52. Kaplan, R.M. and D.P. Saccuzzo, *Psychological Testing: Principles, Applications, and Issues*. 1982: Thomson Brooks/Cole.
53. Kail, R., *Speed of Information Processing Developmental Change and Links to Intelligence.* 2000.
54. Huettel, S.A., A.W. Song, and G. McCarthy, *Functional magnetic resonance imaging*. 2004: Sinauer Associates Sunderland Mass.
55. Xiang, Q., *UBC Physics 542 Lecture Notes*. 2004.
56. Bloch, F., *Nuclear Induction.* Physical Review, 1946. **70**(7-8): p. 460.
57. Meiboom, S. and D. Gill, *Modified Spinâ€ Echo Method for Measuring Nuclear Relaxation Times.* Review of Scientific Instruments, 1958. **29**: p. 688.
58. Carr, H.Y. and E.M. Purcell, *Effects of diffusion on free precession in NMR experiments.* Phys.Rev, 1954. **94**: p. 630.
59. MacKay, A.L., *UBC Physics 542 Lecture Notes*.
60. Poon, C.S. and R.M. Henkelman, *Practical T2 quantitation for clinical applications.* Journal of magnetic resonance imaging : JMRI, 1992. **2**(5): p. 541.
61. Whittall, K.P., et al., *In vivo measurement of T2 distributions and water contents in normal human brain.* Magnetic resonance in medicine : official journal of the Society of Magnetic Resonance in Medicine / Society of Magnetic Resonance in Medicine, 1997. **37**(1): p. 34.
62. Kolind, S.H., B. Madler, and A.L. MacKay, *Faster myelin imaging in vivo; validation of 3D multi-echo T2-relaxation measurements.* Procedings of the International Society for Magnetic Resonance in Medicine, 2008.
63. Klingberg, T., H. Forssberg, and H. Westerberg, *Increased Brain Activity in Frontal and Parietal Cortex Underlies the Development of Visuospatial Working Memory Capacity during Childhood.* Journal of cognitive neuroscience, 2002. **14**(1): p. 1.